**THE EUROPEAN
PHYSICAL JOURNAL C**

Distinguishability of binary extreme-mass-ratio inspirals in low frequency band

Ye Jiang[1,2,a], Wen-Biao Han[1,2,3,4,b], Xing-Yu Zhong[1,2], Ping Shen[1,2], Zi-Ren Luo[3,4,5], Yue-Liang Wu[3,4,5,6]

[1] Shanghai Astronomical Observatory, Shanghai 200030, China
[2] School of Astronomy and Space Science, University of Chinese Academy of Sciences, Beijing 100049, China
[3] School of Fundamental Physics and Mathematical Sciences, Hangzhou Institute for Advanced Study, UCAS, Hangzhou 310024, China
[4] Taiji Laboratory for Gravitational Wave Universe, University of Chinese Academy of Sciences (Beijing/Hangzhou), Beijing 100049, China
[5] Institute of Mechanics, Chinese Academy of Sciences, Beijing 100190, China
[6] Institute of Theoretical Physics, Chinese Academy of Sciences, Beijing 100190, China

Abstract The inspiral of compact stellar objects into massive black holes are one of the main astrophysical sources for the Laser Interferometer Space Antenna (LISA) and Taiji. These extreme-mass-ratio inspirals (EMRIs) have great potential for cosmology and fundamental physics. A binary extreme-mass-ratio inspiral (b-EMRI) describes the case where binary black holes (BBHs) are captured by a supermassive black hole. The b-EMRIs serve as multi-band gravitational wave sources and provide insights into the dynamics of nuclei and tests of general relativity. However, if the b-EMRIs can be distinguished from the normal EMRIs or not is still not clear. In this work, with a few of assumptions, and using the Teukolsky equation, we calculate the approximate gravitational waves of b-EMRIs and assess their detectability by space-based detectors. We also decouple the secondary object information from the Teukolsky equation, enabling us to calculate the energy fluxes and generate the waveforms more conveniently. Variations in the quadrupole of the binary result in small but non-negligible changes in energy fluxes and waveforms, making it possible to distinguish b-EMRI signals with data analysis. This opens up the potential of using b-EMRIs to test gravity theories and for further astrophysical studies.

1 Introduction

The groundbreaking observation of the first gravitational wave (GW) signal [1] marked a significant turning point in astrophysics, providing unprecedented access to the study of extreme gravitational forces [2,3]. Ground-based detectors have effectively recorded the merging of stellar-mass black holes and neutron stars. But these detectors can only detect GWs with frequencies approximately around 10^2 Hz. By contrast, forthcoming space-based GW detectors like the LISA and Taiji [4,5] will enable the detection of GWs in the millihertz frequency range. The potential of these space-based detectors extends to capturing GWs emanating from a diverse array of astrophysical and cosmological sources [6–8].

EMRIs represent highly compelling sources of GWs for upcoming space-based GW detectors. In an EMRI, a supermassive central object of mass M (henceforth a primary) is orbited by a stellar-mass object of mass m (henceforth a secondary) [7,9,10]. The system exhibits a mass ratio of $q = m/M \sim (10^{-7} - 10^{-4})$, and the secondary object completes approximately $\mathcal{O}(1/q)$ orbits around the primary before its final plunge [11]. This affords an exceptional opportunity to rigorously test general relativity [12–17], the Kerr metric [18,19], and precisely measure the spins and masses of massive black holes [20].

Previous studies have shown that EMRIs can acquire BBHs system as a secondary object [21,22]. Such a system is commonly referred to as a b-EMRI. The difference between b-EMRIs and ordinary EMRIs is unambiguous. Instead of having only one stellar-mass BH, now the system contains two stellar-mass BHs, bound by their self-gravity. A triple system of this nature may form through either the tidal capture of BBHs by a SMBH [22] or the formation and migration of BBHs within the accretion disk of an active galactic nucleus (AGN) [23]. According to Ref. [22], the event rate of such an exceptional case caused by tidal capture is equivalent

[a] e-mail: jiangye@shao.ac.cn

[b] e-mail: wbhan@shao.ac.cn (corresponding author)

Springer

to $(10^{-5} - 10^{-4})\,\mathrm{Gpc^{-3}year^{-1}}$ in the pessimistic case and $0.1\,\mathrm{Gpc^{-3}year^{-1}}$ in the most optimistic one. However, due to the non-negligible lifetime of b-EMRIs, within a spherical volume of $1\,\mathrm{Gpc^3}$ (corresponding to a radial distance of about $600\,\mathrm{Mpc}$), there are, on average, about $0.02 - 20$ b-EMRIs expected during detector's mission duration.

Despite its rarity, it can give rise to intriguing phenomena. In the b-EMRI system, the motion of the binary around the primary produces low-frequency waves ($\sim 10^{-3}\,\mathrm{Hz}$), whereas the merger of the two smaller black holes results in high-frequency waves ($\sim 10^2\,\mathrm{Hz}$). As a result, it represents an ideal target for future multi-band GW astronomy [24,25]. The coordinated observation by space-based and ground-based detectors would enable the identification of these intriguing sources [8], thus providing precise constraints on several aspects of fundamental physics beyond the current limit by more than an order of magnitude. These include the loss of rest mass due to GW radiation, the recoil velocity of the BBHs merger, and the dispersion of GWs across various frequencies [26]. Due to the intense gravitational field produced by supermassive black holes (SMBHs), the high-frequency GWs might undergo redshift [23,27,28], offering an excellent opportunity to investigate GW propagation within the realm of strong gravity and to test the validity of general relativity in extraordinary physical circumstances.

There are various possible methods by which the detector can distinguish between b-EMRI and normal EMRI. If the GW frequency produced by the binary corresponds to a fundamental frequency of the SMBH, it could lead to a resonant excitation of the SMBH. The presence of an amplified quasi-normal mode in the EMRI waveform is a clear indication of this effect [28]. Furthermore, the binary nature of the smaller body introduces a phase shift in the EMRI waveform, which can also serve as an identification feature for b-EMRIs [29]. However, there is no quantitative investigation of the distinguishability between b-EMRIs and EMRIs. This paper aims to show the recognizability of the b-EMRIs from normal EMRIs.

For this target, the BBHs are approximately taken as a mass distribution with spin and mass quadrupole, then use the Mathisson–Papapetrou–Dixon (MPD) equation [30–33] to describe its orbit dynamic. By employing the Teukolsky equation, we numerically calculate the waveforms. Compared to Ref. [28], which focuses on the high frequency GW and quasi-normal mode, they model the small binary as two point particles and consider elliptic orbits around the center of mass for the small binary inner motion. Although this approach can model binary inner motion conveniently and high-frequency GWs, but does not focus on the the orbital motion of the whole binary around the SMBH and the inspiral waveforms of the b-EMRIs. In contrast, we discuss the overall motion of the binary around the SMBH and the waveforms during the inspiral. Therefore we employ the multipole

description in this paper. Of course, our calculation of waveforms may be not rigorous for parameter estimates but it can catch the signals of varied quadrupole moments from the BBHs. This should be enough to analyze the distinguishability of b-EMRIs from EMRIs.

The paper is organized as follows. In Sect. 2, we utilize a multi-polar approximation to calculate the waveform generated by b-EMRIs, which describes the inner structure and orbit motion of the BBHs as a secondary object. The numerical methods employed, including the Teukolsky equation and the adiabatic evolution of the orbit, are discussed in Sect. 3. The results are presented in Sect. 4. Our conclusions and future work are discussed in Sect. 5.

Throughout this study, we adopt geometric units where $G = c = 1$. We also adhere to the positive signature convention $(-, +, +, +)$. For symmetry and antisymmetry notation, round and square brackets are respectively used around pairs of indices. For instance, $T^{(\mu\nu)} = (T^{\mu\nu} + T^{\nu\mu})/2$ and $T^{[\mu\nu]} = (T^{\mu\nu} - T^{\nu\mu})/2$.

2 Binary-EMRIs

The binary-EMRI, as a hierarchical three-body system, exhibits various phenomena, particularly when stellar-mass BBHs merge near an SMBH. It has been suggested that if the BBH's orbit around the SMBH has a period shorter than the observation duration of the BBHs by a space-borne GW observatory, there is a high likelihood of lensing the GW emitted by the BBHs through the SMBH [34]. In this case, the acceleration is induced by the orbital motion of the BBHs around the third body. Moreover, if the BBHs are within the LISA frequency range and its signal can be tracked with a reasonable signal-to-noise ratio (SNR) for several months to several years, the acceleration can also be detected [35,36]. The combination of these two effects can enhance the overall parameter estimation.

There are two possible ways in which such an excellent situation could occur. The first channel involves the tidal capture of BBHs by a SMBH. This occurs when the binary passes close enough to the SMBH for tidal interactions to convert a portion of the binary's kinetic energy into internal potential energy [22]. Another possible way is the formation of BBHs in AGN accretion disc [23]. The event rate of BBHs mergers in AGN accretion discs remains highly uncertain. The possible values for the event rate range from $\mathcal{O}(1)\,\mathrm{Gpc^3year^{-1}}$ [37,38] to as high as $10^4\,\mathrm{Gpc^3year^{-1}}$ [39]. Although the latter channel is generally considered more effective than the former, both channels can potentially bring BH-BHs as close as tens of gravitational radii to the central MBH. Furthermore, due to the circularization induced by gas in AGN accretion discs [40,41], the formation of a circular orbit may be a significant scenario for b-EMRI.

This section focuses on the analysis of the b-EMRI system. The BBHs, in principle, is a system with mass distribution, can be expressed as a series of multipole moment expansion. Therefore, we can take the BBHs as a self-gravitational system with multipole moments. The waveforms of an EMRI can be effectively studied using perturbation theory, which models the small object as perturbing the background metric of a larger BH. In the present work, the perturber is not a single point but a mass distribution with complicated multipole moments. However, it is too difficult to include the multipole moments higher than the quadrupole in the Teukolsky equation. So in this work, only terms up to the quadrupole moment are considered. Under this approximation, the energy-momentum tensor of the object can be expressed as follows [42,43]

$$T^{\alpha\beta} = \int d\tau \frac{\delta^4(x - z(\tau))}{\sqrt{-g}} \left(p^{(\alpha} v^{\beta)} - \frac{1}{3} J^{\gamma\delta\epsilon(\alpha} R^{\beta)}{}_{\epsilon\gamma\delta} \right)$$
$$- \int d\tau \nabla_\gamma \left(S^{\gamma(\alpha} v^{\beta)} \frac{\delta^4(x - z(\tau))}{\sqrt{-g}} \right)$$
$$- \frac{2}{3} \int d\tau \nabla_\gamma \nabla_\delta \left(J^{\delta(\alpha\beta)\gamma} \frac{\delta^4(x - z(\tau))}{\sqrt{-g}} \right),$$
(1)

where $v^\mu = dz^\mu/d\tau$ is the tangent vector along the object's worldline, p^μ is the momentum of the object, $S^{\mu\nu}$ is spin tensor, and $J^{\alpha\beta\gamma\delta}$ is the quadrupole tensor. $S^{\mu\nu}$ and $J^{\alpha\beta\gamma\delta}$ satisfy those symmetry conditions [43]

$$S^{\mu\nu} = S^{[\mu\nu]},$$
(2a)

$$J^{\alpha\beta\gamma\delta} = J^{[\alpha\beta][\gamma\delta]},$$
(2b)

$$J^{\alpha\beta\gamma\delta} = J^{\gamma\delta\alpha\beta},$$
(2c)

$$J^{[\alpha\beta\gamma]\delta} = 0.$$
(2d)

Additionally, due to the significantly smaller size of the compact binary compared to the curvature radius of the supermassive black hole, a multipolar approximation can be employed to describe its orbit dynamic [30–33]. Previous work has pointed out that quadrupole moment is not going to cause significant deviations in orbit dynamics [44]. Thus, we choose to drop the quadrupole moment term on orbit dynamics. Consequently, the MPD equation can be written as follows

$$\frac{p^\mu}{d\tau} = -\frac{1}{2} S^{\rho\sigma} v^\nu R^\mu{}_{\nu\rho\sigma},$$
(3a)

$$\frac{S^{\mu\nu}}{d\tau} = 2 p^{[\mu} v^{\nu]}.$$
(3b)

The equatorial circular motion of spinning secondary has been detailly studied by Ref. [45]. We will use this result to construct our waveforms.

Describing the BBHs only with mass, spin and quadrupole is an approximation, but can capture the main property of binary, i.e., the varied quadrupole moment due to the orbital motion and gravitational radiation. The quadrupole tensor can be written as [43,46]

$$J^{\alpha\beta\gamma\delta} = -\frac{3}{m^2} p^{[\alpha} Q^{\beta][\gamma} p^{\delta]},$$
(4)

where $Q^{\mu\nu}$ is the mass quadrupole tensor, and $m^2 = p_\alpha p^\alpha$. Moreover, in the Newtonian limit and center of mass description [47], we have

$$p^\mu = m v^\mu,$$
(5a)

$$S^{\mu\nu} = \epsilon^{\mu\nu}{}_{\gamma\delta} S^\delta v^\gamma,$$
(5b)

$$Q^{ij} = M^{kl},$$
(5c)

$$Q^{it} = Q^{ti} = 0,$$
(5d)

where $\epsilon_{\alpha\beta\gamma\delta} = \sqrt{-g}\hat{\epsilon}_{\alpha\beta\gamma\delta}$ is the Livi-Civita tensor with the Livi-Civita symbol $\hat{\epsilon}_{\alpha\beta\gamma\delta}$, m is the total mass of the secondary, S^δ, M^{ij} are the angular momentum and mass quadrupole moment of BBHs, respectively.

The orbital evolution of the binary-EMRI can be separated into two parts: the inspiral of binary's center of mass into the SMBH, and the orbital evolution of the inner compact binary itself. Both of them are considered in this work. Now we firstly discuss the inner orbit's evolution of the compact binary. Two compact bodies approach each other due to gravitational radiation. In the leading order post-Newtonian approximation, we have

$$d(t) = d_0 \left(\frac{t_{coal} - t}{t_{coal} - t_0} \right)^{1/4},$$
(6)

where $d(t)$ is the separation between the two bodies, d_0 is the value of $d(t)$ at the initial time t_0, t_{coal} is the time at coalescence. t_{coal} and d_0 satisfy the relationship

$$t_{coal} - t_0 = \frac{5}{256} \frac{d_0^4}{m^2 \mu_r},$$
(7)

where $m = m_1 + m_2$ is the total mass of those two bodies, $\mu_r = m_1 m_2/(m_1 + m_2)$ is the reduced mass. And the phase of the binary $\phi_b(t)$ can be expressed as

$$\phi_b(t) = \left(\frac{t_{coal} - t_0}{5 m_c} \right)^{5/8} - \left(\frac{t_{coal} - t}{5 m_c} \right)^{5/8},$$
(8)

where $m_c = \frac{(m_1 m_2)^{3/5}}{(m_1 + m_2)^{1/5}}$ is the chirp mass, and the initial phase $\phi_b(t_0) = 0$.

With the given evolution of the BBHs, we could discuss about the explicit expressions of Eqs. (5a–5c). Consequently,

if we choose Cartesian coordinates $x^i = \{t, x, y, z\}$, and let the orbit lies in the (x, y) plane, the angular momentum S^i is

$$S^z = \mu_r \omega_b d^2, \tag{9}$$

in the center-of-mass frame while the other components vanish, where $\omega_b = \sqrt{m/d^3}$. The mass quadrupole momentum M^{ij} is given by

$$M^{xx} = \mu_r d^2 \sin^2(\phi_b(t)), \tag{10a}$$

$$M^{yy} = \mu_r d^2 \cos^2(\phi_b(t)), \tag{10b}$$

$$M^{xy} = M^{yx} = -\frac{1}{2}\mu_r d^2 \sin(2\phi_b(t)), \tag{10c}$$

while the other components are zero. Then we will do a base change on Eqs. (9) and (10) to get the expressions in Boyer–Lindquist coordinate (t, r, θ, ϕ). In the equatorial plane $(\theta = \pi/2)$, the results read:

$$S^\mu = (0, 0, -\mu_r \omega_b d^2, 0), \tag{11a}$$

$$M^{\mu\nu} = \mu_r d^2 \begin{pmatrix} 0 & 0 & 0 & 0 \\ 0 & sin^2(\phi - \phi_b) & 0 & \frac{1}{2}\sin 2(\phi - \phi_b) \\ 0 & 0 & 0 & 0 \\ 0 & \frac{1}{2}\sin 2(\phi - \phi_b) & 0 & \cos^2(\phi - \phi_b) \end{pmatrix}. \tag{11b}$$

3 Numerical calculations

In this section, we briefly describe the numerical methods used to calculate the waveform $h(t)$.

Due to the extreme mass-ratio, we treat the compact binary as a perturbation on the Kerr spacetime background. This system gradually dissipates energy during its evolution, resulting in shrinking of orbital radius. We employ the adiabatic approximation to model the orbit evolution, which is expressed as:

$$\frac{dE_{\text{orbit}}}{dt} = -\left\langle \frac{dE_{\text{GW}}}{dt} \right\rangle, \tag{12}$$

where $\langle \bullet \rangle$ represents averaging over a time period larger than the orbital time scale $T_o \sim M$ but shorter than the dissipative time scale $T_d \sim T_o/q$ [11,48]. Since the adiabatic approximation breaks down at the innermost stable circular orbit (ISCO) which radius denotes r_{ISCO} [11], our orbit evolution ceases at r_{ISCO}. For all waveform calculations, we select the initial point of the inspiral at $r_{\text{ini}} = 10$.

3.1 Teukolsky equation

In order to study the GW energy and waveform caused by b-EMRIs, we adopt Teukolsky formalism [49]. This method perturbates the weyl scalar

$$\Psi_4 = -C_{\alpha\beta\gamma\delta} n^\alpha \bar{m}^\beta n^\gamma \bar{m}^\delta, \tag{13}$$

where $C_{\alpha\beta\gamma\delta}$ is Weyl tensor, n^α and $\bar{m}^\beta$ are part of the orthonormal null tetrad, the expression of which is given in Eq. (A.14). At infinity, the two GW polarizations are both encoded in the Ψ_4:

$$\Psi_4(r \to \infty) = \frac{1}{2}\frac{\partial^2}{\partial t^2}(h_+ - ih_\times) \tag{14}$$

Teukolsky showed that Ψ_4 could be decomposed as follows in Boyer–Lindquist coordinates [49]

$$\Psi_4 = \rho^4 \sum_{l=2}^{\infty} \sum_{m=-l}^{l} \int_{-\infty}^{\infty} d\omega R_{lm\omega}(\hat{r}) S_{lm}^{\hat{a}\omega}(\theta) e^{i(m\phi - \omega\hat{t})}, \tag{15}$$

where $\rho = 1/(\hat{r} - i\hat{a}\cos\theta)$ and $S_{lm}^{\hat{a}\omega}(\theta)$ is the spin-weighted spheroidal harmonics with weight -2 which satisfies the angular Teukolsky equation

$$\left[\frac{1}{\sin\theta}\frac{d}{d\theta}\left(\sin\theta\frac{d}{d\theta} \right) - \hat{a}^2\omega^2 \sin^2\theta - \left(\frac{m - 2\cos\theta}{\sin\theta} \right)^2 \right.$$
$$\left. + 4\omega\cos\theta - 2 + 2\hat{a}m\omega + \lambda_{lm\omega} \right]_{-2} S_{lm}^{\hat{a}\omega}(\theta) = 0, \tag{16}$$

where $\lambda_{lm\omega} = E_{lm\omega} - 2ma\omega + \hat{a}^2\omega^2 - 2$. And the eigenvalues and eigenfunctions of the angular Teukolsky equation satisfy the relationships $\lambda_{lm-\omega} = \lambda_{l-m\omega}$ and

$$S_{l-m}^{-\hat{a}\omega}(\theta) = (-1)^l S_{lm}^{\hat{a}\omega}(\pi - \theta). \tag{17}$$

The radial function $R_{lm\omega}$ satisfies the following equation

$$\Delta^2 \frac{d}{d\hat{r}}\left(\frac{1}{\Delta}\frac{dR_{lm\omega}}{d\hat{r}} \right) - V(\hat{r})R_{lm\omega} = \mathcal{T}_{lm\omega}, \tag{18}$$

where

$$V(\hat{r}) = -\frac{K^2 + 4i(\hat{r} - 1)K}{\Delta} + 8i\omega\hat{r} + \lambda_{lm\omega}, \tag{19}$$

$$K = (\hat{r}^2 + \hat{a}^2)\omega - \hat{a}m \tag{20}$$

and $\mathcal{T}_{lm\omega}$ is the source term which is given in Eq. (A.1).

The radial Teukolsky equation can be solved through the Green function method [50,51]. We construct the Green function by the linearly independent solutions of homogeneous

radial Teukolsky equation $R_{lm\omega}^{in}$ and $R_{lm\omega}^{up}$, which satisfy those bound conditions

$$R_{lm\omega}^{in} \sim \begin{cases} B_{lm\omega}^{out} \hat{r}^3 e^{i\omega r_*} + B_{lm\omega}^{in} \frac{1}{\hat{r}} e^{-i\omega r_*}, & \hat{r} \to \infty \\ B_{lm\omega}^{tran} \Delta^2 e^{-i\kappa r_*}, & \hat{r} \to r_+ \end{cases} \quad (21a)$$

$$R_{lm\omega}^{up} \sim \begin{cases} D_{lm\omega}^{tran} \hat{r}^3 e^{i\omega r_*}, & \hat{r} \to \infty \\ D_{lm\omega}^{out} \hat{r}^3 e^{i\kappa r_*} + D_{lm\omega}^{in} \Delta^2 e^{-i\kappa r_*}, & \hat{r} \to r_+ \end{cases} \quad (21b)$$

where $\kappa = \omega - m\hat{a}/(2r_+)$ and r_* is the tortoise coordinate of the Kerr metric

$$r_* = \hat{r} + \frac{2r_+}{r_+ - r_-} \ln\left(\frac{\hat{r} - r_+}{2}\right) - \frac{2r_-}{r_+ - r_-} \ln\left(\frac{\hat{r} - r_-}{2}\right) \quad (22)$$

with $r_\pm = 1 \pm \sqrt{1 - \hat{a}}$. The solution of the radial Teukolsky equation with the correct asymptotics reads

$$R_{lm\omega}(\hat{r}) = \frac{1}{W} \left(R_{lm\omega}^{up}(\hat{r}) \int_{r_+}^{\hat{r}} dr' \frac{R_{lm\omega}^{in}(\hat{r}') \mathcal{T}_{lm\omega}(\hat{r}')}{\Delta^2} \right.$$
$$\left. + R_{lm\omega}^{in}(\hat{r}) \int_{\hat{r}}^{\infty} dr' \frac{R_{lm\omega}^{up}(\hat{r}') \mathcal{T}_{lm\omega}(\hat{r}')}{\Delta^2} \right) \quad (23)$$

with the constant Wronskian given by

$$W = \frac{R_{lm\omega}^{in} \partial_r R_{lm\omega}^{up} - R_{lm\omega}^{up} \partial_r R_{lm\omega}^{in}}{\Delta} = 2i\omega B_{lm\omega}^{in} D_{lm\omega}^{tran}. \quad (24)$$

The solution should satisfy the pure outgoing condition at infinity and the pure ingoing condition at the horizon:

$$R_{lm\omega} \sim \begin{cases} Z_{lm\omega}^H \hat{r}^3 e^{i\omega r_*}, & \hat{r} \to \infty \\ Z_{lm\omega}^\infty \Delta^2 e^{-i\kappa r_*}, & \hat{r} \to r_+ \end{cases} \quad (25)$$

with

$$Z_{lm\omega}^{H,\infty} = C_{lm\omega}^{H,\infty} \int_{r_+}^{\infty} \frac{R_{lm\omega}^{in,up}(\hat{r}')}{\Delta^2} \mathcal{T}_{lm\omega}(\hat{r}') d\hat{r}', \quad (26)$$

where

$$C_{lm\omega}^H = \frac{1}{2i\omega B_{lm\omega}^{in}}, \quad C_{lm\omega}^\infty = \frac{B_{lm\omega}^{tran}}{2i\omega B_{lm\omega}^{in} D_{lm\omega}^{tran}}. \quad (27)$$

The amplitudes $Z_{lm\omega}^{H,\infty}$ fully determine the asymptotic GW fluxes at infinity and the horizon. With the energy-momentum tensor presented in Eq. (1), $Z_{lm\omega}^{H,\infty}$ will take the following form

$$Z_{lm\omega}^{H,\infty} = C_{lm\omega}^{H,\infty} \int_{-\infty}^{\infty} d\hat{t} e^{i(\omega\hat{t} - m\phi(\hat{t}))} I_{lm\omega}^{H,\infty}[\hat{r}(\hat{t}), \theta(\hat{t})], \quad (28)$$

where

$$I_{lm\omega}^{H,\infty}[\hat{r}(\hat{t}), \theta(\hat{t})] = \left(\frac{d\hat{t}}{d\lambda}\right)^{-1} \left(C_0 + C_1 \frac{d}{d\hat{r}} + C_2 \frac{d^2}{d\hat{r}^2} \right.$$
$$\left. + C_3 \frac{d^3}{d\hat{r}^3} + C_4 \frac{d^4}{d\hat{r}^4}\right) R_{lm\omega}^{in,up}(\hat{r})|_{\hat{r}(\hat{t}), \theta(\hat{t})}. \quad (29)$$

Detailed expressions of $\{C_i\}_{i \in \{0,1,2,3,4\}}$ can be found in the Appendix A. We care about the situation in which orbits are equatorial and circular. In this case, the form of the source term is greatly simplified, and since $\phi(\hat{t}) = \hat{\Omega}\hat{t}$, $\phi_b(\hat{t}) = \hat{\omega}_b\hat{t}$, $Z_{lm\omega}^{H,\infty}$ will have the following form by adopting the Eq. (B.37):

$$Z_{lm\omega}^{H,\infty} = \delta(\omega - m\hat{\Omega})\mathcal{A}_{lm\omega}^{H,\infty}$$
$$+ \delta(\omega - m\hat{\Omega} - 2(\hat{\omega}_b - \hat{\Omega}))\mathcal{B}_{0lm\omega}^{H,\infty}$$
$$+ \delta(\omega - m\hat{\Omega} + 2(\hat{\omega}_b - \hat{\Omega}))\mathcal{B}_{1lm\omega}^{H,\infty}, \quad (30)$$

with $\mathcal{A}_{lm\omega}^{H,\infty} = 2\pi C_{lm\omega}^{H,\infty} I_{lm\omega}^{H,\infty}[\hat{r}_0, \pi/2]$ at a specific orbital radius $\hat{r}_0$. Then the waveform will become

$$h_+ - ih_\times \sim \sum_{lm} \frac{\mathcal{A}_{lm\omega}^\infty}{(m\hat{\Omega})^2} e^{im\hat{\Omega}(r_* - \hat{t})} S_{lm}^{\hat{a}\omega}(\theta) e^{im\phi}. \quad (31)$$

Here, we only retain the first term of Eq. (30). We dropped the last two terms which correspond the high frequency GWs of the small binary, because these GWs are out of the LISA band.

If we place Eq. (31) into $(dE/dAdt)^\infty \equiv \langle (\dot{h}_+)^2 + (\dot{h}_\times)^2 \rangle / 16\pi$, and use the normalization condition of the spin-weighted spheroidal harmonics, the GW flux at infinity will be obtained by integrating the fluxes over the solid angle, which yields

$$\left(\frac{dE}{dt}\right)_{GW}^\infty = \sum_{l=2}^{\infty} \sum_{m=1}^{l} \frac{|\mathcal{A}_{lm\omega}^H|^2}{2\pi(m\hat{\Omega})^2}, \quad (32)$$

where the sum over m goes for $m = 1, \ldots, l$ since $Z_{lm\omega}^{H,\infty} = (-1)^l \bar{Z}_{lm\omega}^{H,\infty}$ and the bar denotes complex conjugation. Similarly, the GW flux at the horizon is [52,53]

$$\left(\frac{dE}{dt}\right)_{GW}^H = \sum_{l=2}^{\infty} \sum_{m=1}^{l} \frac{\alpha_{lm}|\mathcal{A}_{lm\omega}^\infty|^2}{2\pi(m\hat{\Omega})^2}, \quad (33)$$

where

$$\alpha_{lm} = \frac{256(2r_+)^5 \kappa(\kappa^2 + 4\sigma^2)(\kappa^2 + 16\sigma^2)(m\hat{\Omega})^3}{|C_{lm}|^2} \quad (34)$$

with $\sigma = \sqrt{1 - \hat{a}^2}/(4r_+)$, and

$$
\begin{aligned}
|C_{lm}|^2 = &((\lambda_{lm\hat{\Omega}} + 2)^2 + 4m\hat{a}(m\hat{\Omega}) - 4\hat{a}^2(m\hat{\Omega})^2)(\lambda^2_{lm\hat{\Omega}} \\
& + 36m\hat{a}(m\hat{\Omega}) - 36\hat{a}^2(m\hat{\Omega})^2) \\
& + (2\lambda_{lm\hat{\Omega}} + 3)(96\hat{a}^2(m\hat{\Omega})^2 - 48m\hat{a}(m\hat{\Omega})) \\
& + 144(m\hat{\Omega})^2(1 - \hat{a}^2).
\end{aligned} \tag{35}
$$

3.2 Orbital evolution and waveform

With the expressions of energy radiation at the horizon and infinity in Eqs. (32) and (33), we can get the total GW energy flux by the following equation.

$$
\begin{aligned}
\mathcal{F} &= \left(\frac{dE}{dt}\right)_{\mathrm{GW}} \\
&= \left(\frac{dE}{dt}\right)^{\mathrm{H}}_{\mathrm{GW}} + \left(\frac{dE}{dt}\right)^{\infty}_{\mathrm{GW}} \\
&= \sum_{l=2}^{\infty}\sum_{m=1}^{l}(2\pi(m\omega)^2)^{-1}(|\mathcal{A}^{\mathrm{H}}_{lm\omega}|^2 + \alpha_{lm}|\mathcal{A}^{\infty}_{lm\omega}|^2).
\end{aligned} \tag{36}
$$

Now we can calculate the adiabatic evolution of the orbital radius $r(\hat{t})$ and phase $\phi(\hat{t})$ due to radiation losses as follows

$$
\frac{d\hat{r}}{d\hat{t}} = -q\hat{\mathcal{F}}\left(\frac{d\hat{E}_{\mathrm{orbit}}}{d\hat{r}}\right)^{-1}, \tag{37a}
$$

$$
\frac{d\phi}{d\hat{t}} = \hat{\Omega}(\hat{r}(\hat{t})). \tag{37b}
$$

where $\hat{\mathcal{F}}$ is the normalized flux $\mathcal{F}/q^2$, q is the mass ratio. Finally, we can get the waveform [53]

$$
h_{lm} = -\frac{2}{R}\frac{1}{(m\hat{\Omega})^2}\mathcal{A}^{\mathrm{H}}_{lm\hat{\Omega}}S^{a\hat{\Omega}}_{lm}(\Theta)e^{im[\Phi-\phi(\hat{t})]} \tag{38}
$$

at mode lm, where R is luminosity distance, Θ is the angle between an observer's line of sight and the primary's spin axis, and Φ is the azimuthal angle.

3.3 Decoupling the energy flux and waveform

In the normal EMRIs, usually taking the secondary object as a point particle, the energy fluxes and waveforms can be computed effectively by interpolation from a few of Teukolsky-based numerical data for circular orbits [54], because the inhomogeneous solutions of Teukolsky equation are fully determined by the orbital frequency and perturbed black hole itself. However, in the case of the secondary object with internal structure (extended body, or binary in this work), the solutions depend not only on the black hole but also on the information of the secondary object (spin, quadrupole, etc.). This

induces that one needs to numerically calculate the Teukolsky equation at every time step to evolve the orbit (Eq. (37)) and generate the waveforms (Eq. (38)). Such computation is quite expensive.

To address this issue, we first find that the Teukolsky formalism enables the separation of information between the secondary object and the perturbed field Ψ_4 during the quasicircular inspiral (A more general decoupling formalism will be presented in the paper by some of us [55].). In other words, we can express the GW energy flux and waveform as follows

$$
\mathcal{F} = \sum_{ij}\theta_i\theta_j f_{ij}(\hat{r}), \tag{39}
$$

$$
h_{lm} = \frac{2}{R}\left\{\sum_i \theta_i \mathcal{A}_{ilm}[\hat{r}(t)]\right\} S^{a\hat{\Omega}}_{lm}(\Theta)e^{im[\Phi-\phi(\hat{t})]}, \tag{40}
$$

where $\theta_i = (m, S^\mu, M^{rr}, M^{r\phi}, M^{\phi\phi}, \ldots)$ are the intrinsic parameters of the secondary object and the coefficients

$$
\begin{aligned}
f_{ij}(\hat{r}) = &\sum_{l=2}^{\infty}\sum_{m=1}^{l}\frac{2\pi}{(m\hat{\Omega})^2} \\
&\times \left\{\left[(C^{\mathrm{H}}_{lm\hat{\Omega}}C^{\mathrm{in}}_{ilm\hat{\Omega}}) \diamond (C^{\mathrm{H}}_{lm\hat{\Omega}}C^{\mathrm{in}}_{jlm\hat{\Omega}})\right] \right. \\
&\left. + \alpha_{lm}\left[(C^{\infty}_{lm\hat{\Omega}}C^{\mathrm{up}}_{ilm\hat{\Omega}}) \diamond (C^{\infty}_{lm\hat{\Omega}}C^{\mathrm{up}}_{jlm\hat{\Omega}})\right]\right\},
\end{aligned} \tag{41}
$$

$$
\mathcal{A}_{ilm}(\hat{r}(\hat{t})) = \frac{2\pi}{(m\hat{\Omega})^2}C^{\mathrm{H}}_{lm\hat{\Omega}}C^{\mathrm{in}}_{ilm\hat{\Omega}}[\hat{r}(\hat{t})] \tag{42}
$$

are independent with θ_i. Detailed discussion on the separation form and the analytical expression of $C^{\mathrm{up,in}}_{ilm\hat{\Omega}}$ can be found in Appendix B. Now, the above decomposition forms f_{ij} and $\mathcal{A}_{ilm}$ are independent of the secondary object. Therefore they can be interpolated from just a few numerical points. The numerical solutions of Eqs. (37, 40) can be obtained with the same speed as in the case of test particles.

Now we conclude how we perform our numerical calculations. The solutions $R^{\mathrm{in}}_{lm\omega}$ and $R^{\mathrm{up}}_{lm\omega}$ to the homogeneous Teukolsky equation can be computed using two different methods, MST method [56–58] and solving the SN equation [59]. Since the MST method is typically faster and more accurate than directly solving the SN equation, it will be employed in our calculation. Following the Ref. [44], we truncate the infinite sum in Eq. (41) at $l = 20$ to get the separation coefficients f_{ij}. Choose the parameters of BBHs, compute the energy fluxes $\mathcal{F}$, and solve Eq. (37) numerically. With $r(t)$ and $\phi(t)$ in our hand, we can get the waveform from Eq. (40). Moreover, if the separation distance of BBHs is smaller than its ISCO, we will consider the BBHs have merged and switch to the calculation of normal EMRI waveforms.

4 Waveforms and data analysis

In this section, we examine whether we can distinguish b-EMRI signals from normal EMRI ones. Given two time series $h_1(t)$ and $h_2(t)$, the maximized fitting factor (match) between them is defined as follows [60,61]:

$$\mathcal{M}(h_1, h_2) = \max_{t_s, \phi_s} \frac{\langle h_1(t)|h_2(t+t_s)e^{i\phi_s}\rangle}{\sqrt{\langle h_1|h_1\rangle\langle h_2|h_2\rangle}}, \quad (43)$$

and the $\langle h_1|h_2\rangle$ is defined by:

$$\langle h_1|h_2\rangle = \int_0^\infty \frac{\hat{h}_1(f)\hat{h}_2(f)}{S_n(f)} df, \quad (44)$$

where $\hat{h}(f)$ is the Fourier transform of $h(t)$, and $S_n(f)$ is the power spectrum density (PSD) of the detector. We use PyCBC [62] to calculate the match Eq. (43) which quantifies the differences between the b-EMRI signals and the normal EMRI ones. Here for simplicity without loss of generality, we only consider the dominant mode $l = m = 2$.

Additionally, in order to avoid the tidal disruption of the inner binary by the SMBH, we require the initial separation of the binary satisfies the following condition

$$\frac{2M(m_1+m_2)d}{r^3} \Big/ \frac{m_1 m_2}{d^2} \lesssim 10^{-1}, \quad (45)$$

where d is the separation of two stellar mass black holes, and r is the orbit radius of the outer orbit (the separation between the inner binary to the SMBH).

For b-EMRIs, while the compact binary inspirals into the SMBH, the orbital angular momentum and evolving quadrupole produce different source term in the Teukolsky equation compared to the case of normal EMRIs. Therefore, the energy fluxes and waveforms from b-EMRIs could deviate from the one of EMRIs.

The two BHs in the compact binary may merge during the binary inspiraling into the SMBH. The mass of the remnant will be smaller than the initial mass of the binary due to the merger. The mass-loss ratio ($\mathcal{R} \equiv (1-m_{\text{final}}/(m_1+m_2))$) is about 5% in the BBH mergers [63–65]. This sudden change of mass will induce a tiny "jump" in the GW signal and in principle make the recognition of b-EMRI easier.

Figure 1 shows the 1-year waveform h_+ of the b-EMRI, where the BBHs merge at the 6th month, and a normal EMRI with a secondary mass equal to that of the BBHs in the b-EMRI. Once the BBHs have merged, the b-EMRI becomes a normal EMRI but with a sudden change of the secondary mass. According to Eq. (37), for EMRIs we can find the inspiral time scale $t_{\text{inspiral}} = q^{-1}D(\hat{r})$, where $D(\hat{r}) = \int \mathcal{F}^{-1}(d\hat{E}_{\text{orbit}}/d\hat{r})d\hat{r}$, then we can get $t_{\text{inspiral}} \propto q^{-1}$. Therefore, due to the mass loss, the waveform of b-EMRI dif-

fers obviously from the normal EMRI after the merger (see Fig. 1). Furthermore, in Fig. 2, we show the case that the compact binary does not merge during the 1-year inspiral. Without the mass loss, the waveforms from b-EMRI and normal EMRI superpose together and can not be distinguished visually (see the bottom panel of Fig. 2). However, if we zoom in the waveforms, we still can see the obvious dephasing between them with enough evolution time (see the top panels of Fig. 2). The dephase can be larger than 1 radian, which in principle can be recognized by matched filtering.

In Fig. 3, we show the matches between the normal EMRIs and b-EMRIs with different merger moment of the compact binaries. As a result, we may state that b-EMRIs with compact binary mergers can be recognized from normal EMRIs easily. Fortunately, even for the b-EMRIs without the merger, the match between two kinds of waveforms is small enough to distinguish the b-EMRI signals. At the same time, the merger of the compact object also radiates high frequency GWs which can be observed by LIGO, Virgo and KAGRA, or the third generation detectors like Einstein Telescope and Cosmic Explorer. This makes the b-EMRIs become multi-band GW sources, as stated in [22,26].

Though from Fig. 3, the matchs are small enough to distinguish two kinds of waveforms, the "confusion problem" is one challenge we may encounter in recognizing the b-EMRIs from normal EMRIs. This kind of confusion is intrinsic to the model, namely, a b-EMRI waveform and an EMRI one with different parameters can be almost identical. If the confusion problem exists, even if the ground-based detectors observe the GW signals from the merger of BBHs in b-EMRI, we may still have a challenge to relate it with the b-EMRI event. In addition, in a pessimistic scenario, the high-frequency signals may be missed by the ground-based detectors. Hence, an important question arises, i.e., whether the space-borne detectors can distinguish a b-EMRI from normal EMRIs. With this question in mind, we performed a confusion test on the b-EMRI waveforms in both cases (merger or non-merger) to explore whether a b-EMRI waveform can be replaced with an EMRI one. The results are demonstrated in Fig. 4. Note that here for efficiency we omit the spin in the orbital motion, because with or without spin only has a tiny change on the match values, and no influence on the result. In the left panel, the merger of the black holes in b-EMRI occurs after 6 months, and the maximum match $\mathcal{M}_{\text{max}} = 0.861$. In the right panel, the compact binary does not merge during the one-year inspiral, then $\mathcal{M}_{\text{max}}$ is 0.982. If the mismatch $1 - \mathcal{M} > (N-1)/(2\rho^2)$, a certain signal in principle can be distinguished [66], where N is the number of parameters and ρ is the SNR. For typical EMRIs, usually $N = 14$, the threshold of $\mathcal{M} = 0.984$ for SNR reaches 20. Therefore, LISA or Taiji in principle can recognize the b-EMRIs from normal EMRIs with enough SNRs even for the non-merger cases.
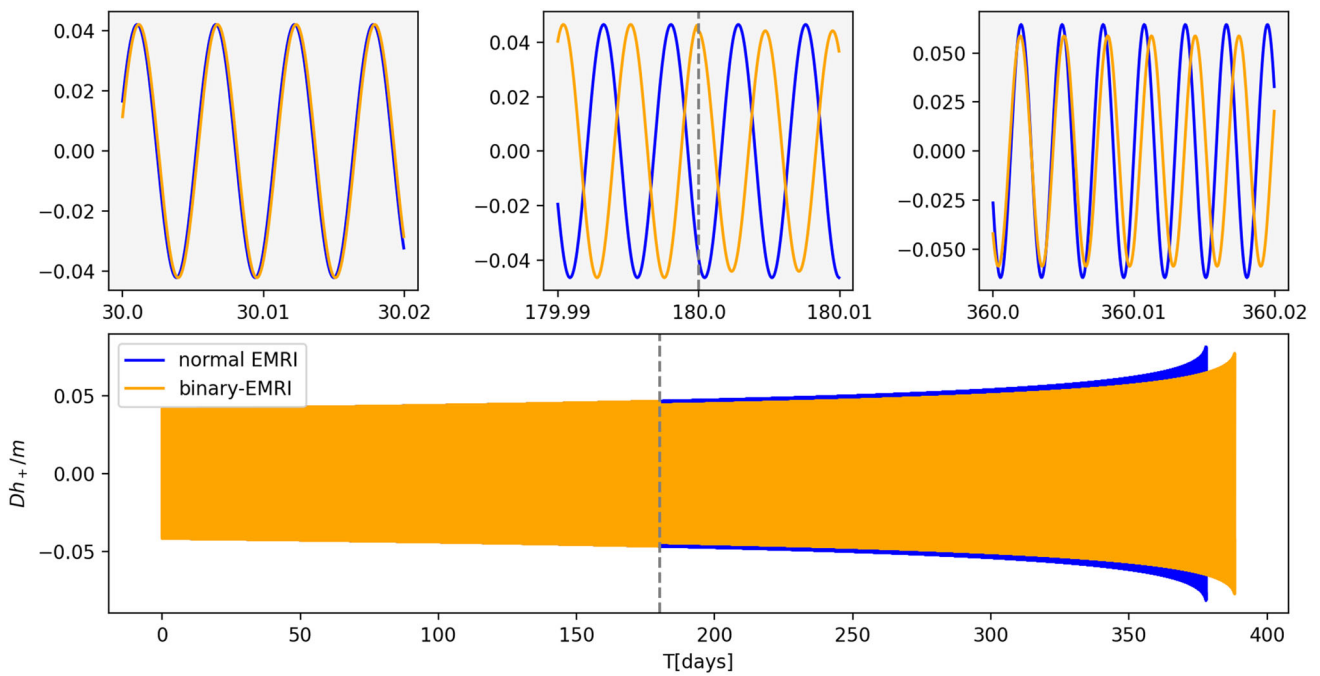
Fig. 1 The $l = 2$, $m = 2$ waveform h_+ of the b-EMRI with parameters $m_1 = m_2$, $m_1/M = 10^{-5}$, $\hat{a} = 0.3$, $\mathcal{R} = 5\%$, alongside a normal EMRI waveform with parameters $m' = m_1 + m_2$, $\hat{a} = 0.3$, $l = 2$, $m = 2$. The compact binary of the b-EMRI mergers in the sixth month, indicated by the dashed line
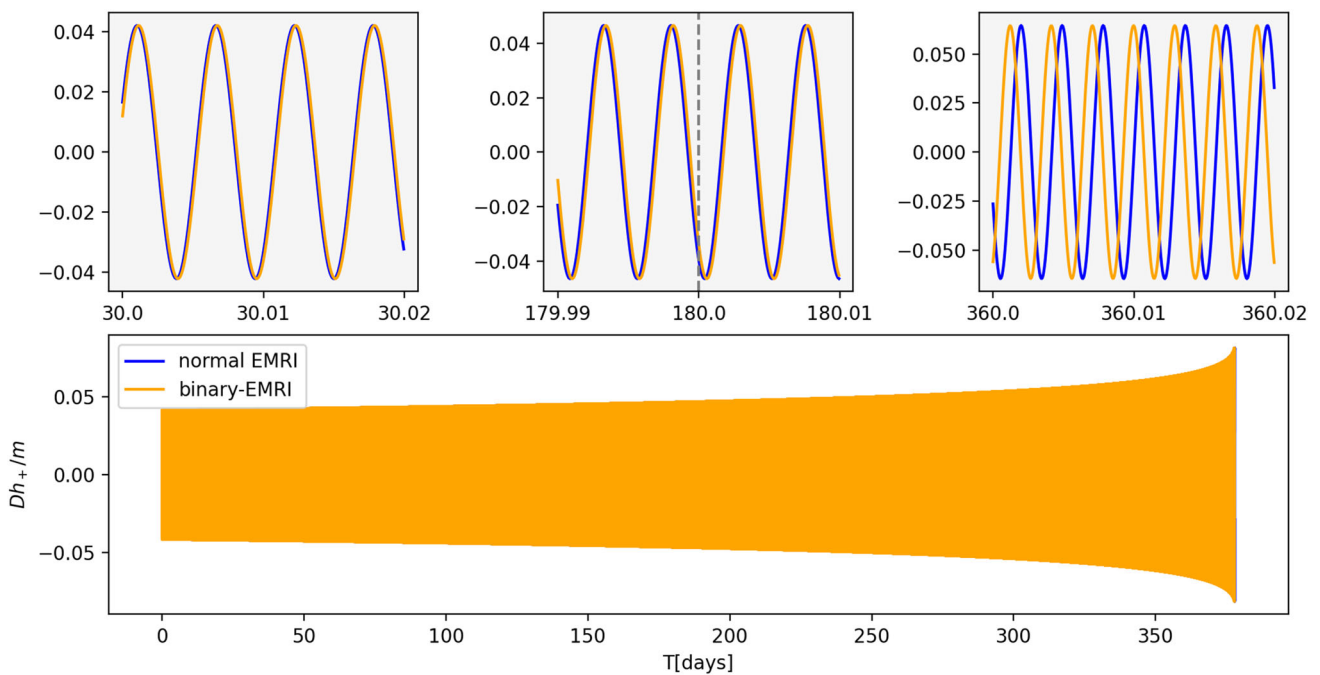
Fig. 2 The $l = 2$, $m = 2$ waveform h_+ of the b-EMRI with parameters $m_1 = m_2$, $m_1/M = 10^{-5}$, $d_0 = 0.029M$, $\hat{a} = 0.3$ and the waveform of normal EMRI with the same parameters in Fig. 1. The compact binary in the b-EMRI does not merge during this 1-year inspiral
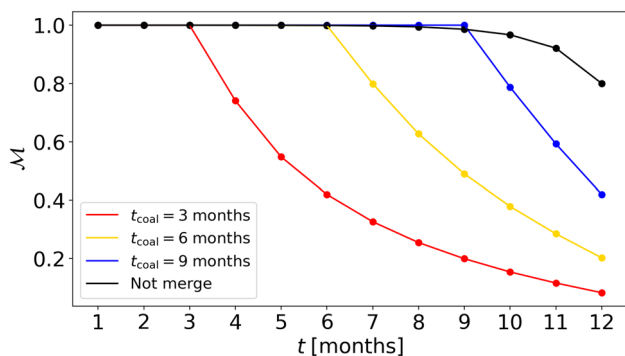
Fig. 3 This figure shows the matchs between the waveforms of b-EMRIs and normal EMRIs for different binary coalescence times. The black line denotes no merger case with initial separation $d_0 = 0.28\,M$. The parameter fixed at $\hat{a} = 0.3$, $m_1 = m_2$, $m_1/M = 10^{-5}$ for b-EMRIs, and $m = m_1 + m_2$ for normal EMRIs. We take time series of different lengths from 1 month to 12 months to calculate matchs. In the not merger case, $\mathcal{M} = 0.80$ at 12 months

For further quantifying the recognition of b-EMRIs, we calculate Bayesian factors of b-EMRI versus EMRI waveforms with a simple linearized analysis by following the method of Moore et al. [67]. Bayes factor is used in Bayesian hypothesis testing to quantify the evidence in favor of one hypothesis compared to another. For the combined parameter space $\lambda = (\alpha; \theta)$, the observed signal, s, can be described as the sum of the GW signal and the detector noise:

$$s = n + h(\alpha; \theta) = n + h(\alpha_{\mathrm{Tr}}; \theta_{\mathrm{Tr}}) + \Delta h(\theta_{\mathrm{Tr}}), \quad (46)$$

where, parameter α represents the derivation of the secondary object from a single compact object, and in the case of normal EMRI, α is equal to 0. θ denotes the normal EMRI parameters including both intrinsic (masses, spins, etc.) and extrinsic

(distance, sky position, etc.) ones. $\Delta h(\theta_{\mathrm{Tr}})$ represents the modelling error.

Assuming the instrumental noise is Gaussian, the likelihood $\mathcal{L}(\alpha; \theta) \equiv P(s|\alpha; \theta)$ is given by

$$\ln \mathcal{L}(\alpha; \theta) = -\frac{1}{2}|s - h(\alpha; \theta)|^2 + c$$
$$= -\frac{1}{2}|s - \delta h(\alpha; \theta) + \Delta h(\theta_{\mathrm{Tr}})|^2 + c, \quad (47)$$

where $|\bullet|^2 \equiv \langle \bullet | \bullet \rangle$, $\delta h(\alpha; \theta) = h(\alpha; \theta) - h(\alpha_{\mathrm{Tr}}; \theta_{\mathrm{Tr}})$ and c is an unimportant normalization constant. For simplicity, we assume that the prior on λ is flat, so the posterior is proportional to the likelihood. Through the first-order Taylor expansion of δh, the log-likelihood expanded at the maximum likelihood (ML) parameters λ_{ML} is given by

$$\ln \mathcal{L}(\lambda) = c' - \frac{1}{2}\Gamma_{\mu\nu}(\lambda - \lambda_{\mathrm{ML}})^\mu (\lambda - \lambda_{\mathrm{ML}})^\nu \quad (48)$$

where c' is another constant, $\Gamma_{\mu\nu}$ is the Fisher matrix. For the binary-EMRI, the Bayesian evidence integral is

$$Z_{\mathrm{binary}} = \int d\lambda \mathcal{L}(\lambda) = e^{c'}\sqrt{\frac{(2\pi)^{k+1}}{\det \Gamma_{\mu\nu}}}, \quad (49)$$

where k is the number of parameters θ. For the normal EMRI, $\alpha = 0$, we have

$$\ln \mathcal{L}_{\mathrm{normal}}(\theta) = c' - \frac{1}{2}\Gamma_{00}\alpha_{\mathrm{ML}}$$
$$- \frac{1}{2}\Gamma_{ij}(\theta - \theta_{\mathrm{ML}})^i (\theta - \theta_{\mathrm{ML}})^j \quad (50)$$

$$Z_{\mathrm{normal}} = \int d\theta \mathcal{L}_{\mathrm{normal}}(\theta) = e^{c' - \Gamma_{00}\alpha_{\mathrm{ML}}^2/2}\sqrt{\frac{(2\pi)^k}{\det \Gamma_{\mu\nu}}} \quad (51)$$
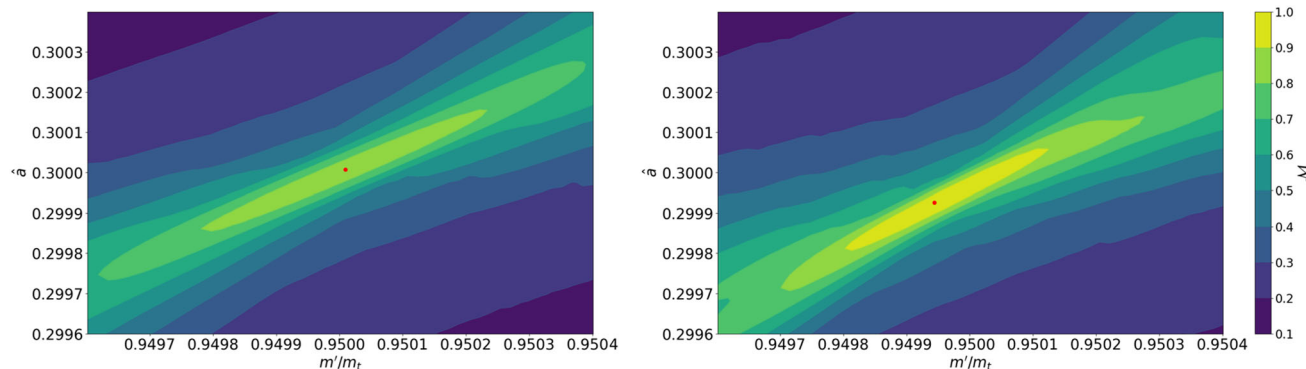

Fig. 4 Distribution of the match between a b-EMRI waveform and normal EMRI waveforms with varied $\hat{a}$ and m'. Here, $\hat{a}$ represents the primary's dimensionless spin, m' the mass of the secondary in normal EMRIs, and m_b the mass of the compact binary in the b-EMRI. In the left panel, the compact binary in b-EMRI mergers at the sixth month

with $m_1 = m_2$, $m_1/M = 10^{-5}$ and $\hat{a} = 0.3$. In the right panel, the compact binary does not merge during this 1-year inspiral, the corresponding initial separation is $d_0 = 0.036M$. The maximum matchs (represented by red points) are 0.861 and 0.982 for the left and right panels respectively

Table 1 The logarithm of the Bayes factors ($\ln \mathcal{B}$) between the waveforms from a b-EMRI and a normal EMRI. The signals continue for one year and start at $r_{\text{start}} = 10\,M$. "–" mean the BBHs do not merge during the one-year signal

	$\hat{a}$	m_1/M	$d_0[M]$	t_{coal}[months]	R[Gpc]	SNR	$1 - \mathcal{M}$	$\ln \mathcal{B}$
1	0.8	2×10^{-5}	3.6×10^{-2}	4	4.0	17.6	9.3×10^{-1}	286.1
2	0.8	9×10^{-6}	3.0×10^{-2}	–	0.6	26	9.1×10^{-2}	69.0
3	0.95	1×10^{-5}	2.8×10^{-2}	–	0.5	34.1	3.6×10^{-2}	39.6
4	0.9	7×10^{-6}	2.0×10^{-2}	9	1.0	10.5	3.1×10^{-1}	33.3
5	0.8	1×10^{-5}	2.4×10^{-2}	6	2.5	7.0	6.5×10^{-1}	32.1
6	0.95	5×10^{-6}	1.5×10^{-2}	7	0.8	8.5	4.5×10^{-1}	31.3
7	0.95	1×10^{-5}	3.6×10^{-2}	–	2.0	8.6	3.8×10^{-1}	26.9
8	0.95	2×10^{-6}	8.1×10^{-3}	10	0.2	12.6	1.4×10^{-1}	20.6
9	0.9	1.1×10^{-5}	3.0×10^{-2}	11	2.0	10.2	1.7×10^{-1}	16.3
10	0.9	4×10^{-6}	1.4×10^{-2}	–	0.3	18.2	2.6×10^{-4}	-1.9
11	0.8	6×10^{-6}	2.0×10^{-2}	–	0.5	18.8	2.6×10^{-5}	-2.0
12	0.9	3×10^{-6}	1.6×10^{-2}	–	0.2	20.0	2.4×10^{-5}	-2.1

where $\alpha_{\text{ML}} = z/\rho + \sqrt{2(1 - \mathcal{M})} \cos \iota$ can be got by the equation

$$\left. \frac{\partial \ln \mathcal{L}}{\partial \lambda} \right|_{\lambda = \lambda_{\text{ML}}} = 0, \tag{52}$$

and $\Gamma_{00} = 1/\rho^2$. Here, $z \sim N(0, 1)$ is the random number associated with the noise realization, and ι is the angle between the signals $\Delta h(\theta_{\text{Tr}})$ and $\partial h/\partial \alpha$. The Bayes factor in favor of the deviation from normal EMRI is

$$\mathcal{B} = \frac{\Pi}{A} \frac{Z_{\text{binary}}}{Z_{\text{normal}}}, \tag{53}$$

where Π is the prior Bayes factor and $A = \alpha_{\text{max}} - \alpha_{\text{min}}$ is the prior range of α. Inserting the expressions in Eqs. (49) and (51) into Eq. (53), the logarithm of the Bayes factor is given by

$$\ln \mathcal{B} = \ln \left(\frac{\Pi}{A} \frac{\sqrt{2\pi}}{\rho} \right) + \frac{(z + \rho \sqrt{2(1 - \mathcal{M})} \cos \iota)^2}{2}. \tag{54}$$

In this work, our results are scaled to $\Pi = A = 1$, $z = 0$, $\cos \iota \to \cos \iota_m = 1$, and the threshold of the Bayes factor $\mathcal{B}_{\text{threshold}} = e^{10}$ [67]. The final expression of $\ln \mathcal{B}$ reads

$$\ln \mathcal{B} = \ln \left(\frac{\sqrt{2\pi}}{\rho} \right) + \rho^2 (1 - \mathcal{M}). \tag{55}$$

In Table 1, we list the logarithm of the Bayes factor ($\ln \mathcal{B}$) for twelve b-EMRI sources and sort them by $\ln \mathcal{B}$. Some of the Bayes factor $\mathcal{B}$ are larger than the threshold $\mathcal{B}_{\text{threshold}}$, which means these b-EMRIs can be recognized from the normal EMRIs. Mass loss due to the merger of BBHs is a distinctive feature of b-EMRIs that can distinguish them from normal EMRIs. This feature makes it easier to recognize b-EMRIs from normal EMRIs. If the BBHs do not merge

during the observation, we may also recognize them as b-EMRIs if with appropriate binary mass m and separation d_0. Because the quadrupole moment of the compact binary is the critical factor for identifying b-EMRIs. This quadrupole moment is decided by the m and d_0 in Eq. (11).

5 Conclusions

Binary-EMRIs can serve as multi-band GW sources for both ground-based and space-borne detectors. In this study, we find that b-EMRIs can be distinguished from normal EMRIs in low frequency band. Due to the several approximations, the accuracy of our b-EMRI waveform may not be sufficient for parameter estimation, but it should be enough to demonstrate its distinguishability for our work.

Though the change of the energy fluxes and waveforms due to the binary is tiny compared with the case of the secondary body just a single black hole, we find that regardless affect whether the BBHs merge or not during the inspiraling around the SMBH. We show that the data analysis can in principle distinguish b-EMRIs and normal EMRIs. Therefore, the future LISA and Taiji detectors can recognize b-EMRIs if this kind of sources exist and have enough SNR. Additionally, we decompose the complicated source terms and can calculate the b-EMRI waveform in just a few seconds with a single CPU core. This method will facilitate the development of the waveform template for parameter estimation.

There are still some difficult problems for future work. Full consideration of dissipative effects in the case of BBHs as secondary bodies would also require consideration of the evolution of BBHs in Kerr spacetime. The elliptical orbit will be caused by the tidal effect, and the energy flux of BBHs will be influenced by Kerr spacetime, which are more dif-

ficult problems to tackle, especially in the case of generic orbits. Once the complete waveform caused by this hierarchical three-body system is known, the high-frequency GW signal from the BBHs can be separated from the whole signal by using high-pass filtering techniques.

Finally, a particularly intriguing venture involves multiband observation for parameter estimation. Space-born GW detectors are capable of identifying b-EMRIs, but the measurement of BBHs may not be very accurate. In the case of identifying a b-EMRI, if ground-based GW detectors can simultaneously find a BBHs merger event associated with this b-EMRI, then we can accurately measure the information of the binary. This makes b-EMRI a typical multi-band gravitational wave source. By exploiting simultaneous observations from space-based and ground-based detectors, the accuracy of parameter estimation can be significantly improved, such as the loss of rest mass result by merger and the detailed information about BBHs. Therefore, the b-EMRI can be a unique laboratory for testing general relativity.

Data Availability Statement Data will be made available on reasonable request. [Authors' comment: The datasets generated during and/or analysed during the current study are available from the corresponding author on reasonable request.]

Code Availability Statement Code/software will be made available on reasonable request. [Author's comment: The code/software generated during and/or analysed during the current study is available from the corresponding author on reasonable request.]

Appendix A: The Teukolsky source term

In this appendix, we will present the main conclusions about source terms containing quadrupole moments. Different from

[44], we abandon projecting the energy-momentum tensor to the orthonormal tetrad. This simplifies the expressions. It is worth pointing out that there are some typos in Eqs. (B10, B11) of [44].

Following the Ref. [45], the source term is given by the following relation

$$\mathcal{T}_{lm\omega} = \int dt d\theta d\phi \Delta^2 \left(\mathcal{T}_{NN} + \mathcal{T}_{\bar{M}N} + \mathcal{T}_{\bar{M}\bar{M}} \right) \tag{A.1}$$

where,

$$\mathcal{T}_{NN} = f_{nn}^0 n_\mu n_\nu T^{\mu\nu}, \tag{A.2}$$

$$\mathcal{T}_{\bar{M}N} = f_{n\bar{m}}^0 n_{(\mu} \bar{m}_{\nu)} T^{\mu\nu} + \partial_r (f_{n\bar{m}}^1 n_{(\mu} \bar{m}_{\nu)} T^{\mu\nu}), \tag{A.3}$$

$$\mathcal{T}_{\bar{M}\bar{M}} = f_{\bar{m}\bar{m}}^0 \bar{m}_\mu \bar{m}_\nu T^{\mu\nu} + \partial_r (f_{\bar{m}\bar{m}}^1 \bar{m}_\mu \bar{m}_\nu T^{\mu\nu})$$
$$+ \partial_r^2 (f_{\bar{m}\bar{m}}^2 \bar{m}_\mu \bar{m}_\nu T^{\mu\nu}) \tag{A.4}$$

with

$$f_{nn}^0 = -\frac{2\sin\theta}{\Delta^2 \rho^3 \bar{\rho}} (\mathcal{L}_1^\dagger - 2ia\sin\theta)\mathcal{L}_2^\dagger S_{lm}^{a\omega}, \tag{A.5}$$

$$f_{n\bar{m}}^0 = \frac{4\sin\theta}{\sqrt{2}\rho^3 \Delta} \left[\left(\frac{iK}{\Delta} + \rho + \bar{\rho} \right) \mathcal{L}_2^\dagger \right.$$
$$\left. - a\sin\theta \frac{K}{\Delta} (\bar{\rho} - \rho) \right] S_{lm}^{a\omega}, \tag{A.6}$$

$$f_{n\bar{m}}^1 = \frac{4\sin\theta}{\sqrt{2}\rho^3 \Delta} [\mathcal{L}_2^\dagger + ia\sin\theta(\bar{\rho} - \rho)] S_{lm}^{a\omega}, \tag{A.7}$$

$$f_{\bar{m}\bar{m}}^0 = \frac{\bar{\rho}}{\rho^3} \left[\frac{d}{dr} \left(\frac{iK}{\Delta} \right) - 2\rho \frac{iK}{\Delta} + \frac{K^2}{\Delta^2} \right] S_{lm}^{a\omega}, \tag{A.8}$$

$$f_{\bar{m}\bar{m}}^1 = -2 \left(\frac{\bar{\rho}}{\rho^2} + \frac{i\bar{\rho}K}{\rho^3 \Delta} \right) S_{lm}^{a\omega}, \tag{A.9}$$

$$f_{\bar{m}\bar{m}}^2 = -\frac{\bar{\rho}}{\rho^3} S_{lm}^{a\omega}, \tag{A.10}$$

where

$$K = ((r^2 + a^2)\omega - am), \tag{A.11}$$

$$\rho = (r - ia\sin\theta)^{-1}, \tag{A.12}$$

$$\mathcal{L}_s^\dagger = \frac{\partial}{\partial \theta} - \frac{m}{\sin\theta} + a\omega\sin\theta + s\cot\theta \tag{A.13}$$

and the null tetrad is defined as

$$l^\mu = \left(\frac{r^2 + a^2}{\Delta}, 1, 0, \frac{a}{\Delta} \right),$$
$$n^\mu = \left(\frac{r^2 + a^2}{2\Sigma}, -\frac{\Delta}{2\Sigma}, 0, \frac{a}{2\Sigma} \right),$$
$$m^\mu = \left(\frac{ia\sin\theta}{\sqrt{2}}, 0, \frac{1}{\sqrt{2}}, \frac{i}{\sqrt{2}\sin\theta} \right) \bigg/ (r + ia\cos\theta). \tag{A.14}$$

Now, we get the new form of energy-momentum tensor as defined in Eq. 1

$$
\begin{aligned}
T^{\mu\nu} = \int d\tau \Bigg[& \frac{1}{\sqrt{-g}} \mathcal{P}^{(\mu\nu)} \delta^4 + \frac{1}{\sqrt{-g}} \partial_\delta \left(\mathcal{Q}^{\delta(\mu\nu)} \delta^4 \right) \\
& + \frac{1}{\sqrt{-g}} \partial_\delta \partial_\rho \left(\mathcal{I}^{\delta(\mu\nu)\rho} \delta^4 \right) \Bigg],
\end{aligned}
$$

(A.15)

where

$$
\begin{aligned}
\mathcal{P}^{\mu\nu} =& P^\mu v^\nu + \Gamma^\mu{}_{\delta\rho} S^{\nu\rho} v^\delta \\
& + \frac{1}{3} J^{\mu\delta\rho\gamma} R^\nu{}_{\delta\rho\gamma} - \frac{2}{3} \Gamma^\mu{}_{\delta\rho} \Gamma^\nu{}_{\gamma\sigma} J^{\delta\gamma\rho\sigma} \\
& - \frac{2}{3} (2\Gamma^{\mu\delta}{}_\rho \Gamma_{\gamma\delta\sigma} J^{\nu(\rho\gamma)\sigma} + J^\mu{}_{\delta\rho\gamma} \partial^\gamma \Gamma^{\nu\delta\rho}),
\end{aligned}
$$

(A.16)

$$
\mathcal{Q}^{\delta\mu\nu} = - S^{\delta\mu} v^\nu - \frac{2}{3} (J^{\rho\mu\nu\gamma} \Gamma^\delta{}_{\rho\gamma} + 2J^{\rho\delta\gamma\mu} \Gamma^\nu{}_{\gamma\rho}),
$$

(A.17)

$$
\mathcal{J}^{\delta\mu\nu\rho} = - \frac{2}{3} J^{\delta\mu\nu\rho}.
$$

(A.18)

To remove Dirac delta functions from $Z_{lm\omega}^{H,\infty}$, we used the well-known property

$$
\int g(x) \frac{d^n[f(x)\delta(x-x_0)]}{dx^n} dx = f(x) \frac{d^n[g(x)]}{dx^n}\Big|_{x=x_0}.
$$

(A.19)

By switching the order of integration, we can obtain the general expression

$$
\begin{aligned}
Z_{lm\omega}^{\infty,H} = C_{lm\omega}^{\infty,H} \int dt \left(\frac{dt}{d\lambda}\right)^{-1} e^{i(\omega t - m\phi)} \\
\times \left(C_0 + C_1 \frac{d}{dr} + C_2 \frac{d^2}{dr^2} + C_3 \frac{d^3}{dr^3} \right. \\
\left. + C_4 \frac{d^4}{dr^4} \right) R_{lm\omega}^{up,in}
\end{aligned}
$$

(A.20)

where

$$
C_0 = \mathcal{O}^{\mu\nu} \left[f_{\mu\nu}^0 \right],
$$

(A.21)

$$
C_1 = -\mathcal{O}^{\mu\nu} \left[f_{\mu\nu}^1 \right] + \mathcal{H}^{\mu\nu} \left[f_{\mu\nu}^0 \right],
$$

(A.22)

$$
C_2 = \mathcal{O}^{\mu\nu} \left[f_{\mu\nu}^2 \right] - \mathcal{H}^{\mu\nu} \left[f_{\mu\nu}^1 \right] + \mathcal{K}^{\mu\nu} \left[f_{\mu\nu}^0 \right],
$$

(A.23)

$$
C_3 = \mathcal{H}^{\mu\nu} \left[f_{\mu\nu}^2 \right] - \mathcal{K}^{\mu\nu} \left[f_{\mu\nu}^1 \right],
$$

(A.24)

$$
C_4 = \mathcal{K}^{\mu\nu} \left[f_{\mu\nu}^2 \right]
$$

(A.25)

with

$$
f_{\mu\nu}^0 = (f_{nn}^0 n_\mu n_\nu + f_{n\bar{m}}^0 n_{(\mu} \bar{m}_{\nu)} + f_{\bar{m}\bar{m}}^0 \bar{m}_\mu \bar{m}_\nu)/\sqrt{-g},
$$

(A.26)

$$
f_{\mu\nu}^1 = (f_{n\bar{m}}^1 n_{(\mu} \bar{m}_{\nu)} + f_{\bar{m}\bar{m}}^1 \bar{m}_\mu \bar{m}_\nu)/\sqrt{-g},
$$

(A.27)

$$
f_{\mu\nu}^2 = (f_{\bar{m}\bar{m}}^2 \bar{m}_\mu \bar{m}_\nu)/\sqrt{-g}
$$

(A.28)

and operators $\mathcal{O}^{\mu\nu}$, $\mathcal{H}^{\mu\nu}$, $\mathcal{K}^{\mu\nu}$ being defined as

$$
\begin{aligned}
\mathcal{O}^{\mu\nu} =& (-\omega^2 \mathcal{J}^{t\mu\nu t} + 2m\omega \mathcal{J}^{t\mu\nu\phi} - m^2 \mathcal{J}^{\phi\mu\nu\phi} \\
& - i\omega \mathcal{Q}^{t\mu\nu} + im\mathcal{Q}^{\phi\mu\nu} + \mathcal{P}^{\mu\nu}) \\
& + (2i\omega \mathcal{J}^{t\mu\nu r} - 2im\mathcal{J}^{r\mu\nu\phi} - \mathcal{Q}^{r\mu\nu})\partial_r \\
& + (2i\omega \mathcal{J}^{t\mu\nu\theta} - 2im\mathcal{J}^{\phi\mu\nu\theta} - \mathcal{Q}^{\theta\mu\nu})\partial_\theta \\
& + 2\mathcal{J}^{r\mu\nu\theta} \partial_r \partial_\theta + \mathcal{J}^{r\mu\nu r} \partial_r^2 + \mathcal{J}^{\theta\mu\nu\theta} \partial_\theta^2,
\end{aligned}
$$

(A.29)

$$
\begin{aligned}
\mathcal{H}^{\mu\nu} =& i(2\omega \mathcal{J}^{t\mu\nu r} - 2m\mathcal{J}^{r\mu\nu\phi} + i\mathcal{Q}^{r\mu\nu}) \\
& + 2(\mathcal{J}^{r\mu\nu r} \partial_r + \mathcal{J}^{r\mu\nu\theta} \partial_\theta),
\end{aligned}
$$

(A.30)

$$
\mathcal{K}^{\mu\nu} = \mathcal{J}^{r\mu\nu r}.
$$

(A.31)

It is convenient to check the correctness of operators $\mathcal{O}^{\mu\nu}$, the form of the terms is related to the direction of the components of the multipole tensor. The direction (t, r, θ, ϕ) represents $(-i\omega, -\partial_r, -\partial_\theta, im)$, respectively. For example, the coefficient of $\mathcal{J}^{\phi(\mu\nu)\theta}$ should be $2(-\partial_\theta)(im)$. And operators $\mathcal{O}^{\mu\nu}$, $\mathcal{H}^{\mu\nu}$, $\mathcal{K}^{\mu\nu}$ satisfy

$$
\begin{aligned}
\mathcal{O}^{\mu\nu}[f(r)g(r,\theta)] = \mathcal{O}^{\mu\nu}[g(r,\theta)]f(r) \\
+ \mathcal{H}^{\mu\nu}[g(r,\theta)]\frac{df(r)}{dr} \\
+ \mathcal{K}^{\mu\nu}[g(r,\theta)]\frac{d^2 f(r)}{dr^2}
\end{aligned}
$$

(A.32)

where $g(r,\theta)$ and $f(r)$ are arbitrary smooth functions.

Appendix B: Parameter separation

In this appendix, We will give an explicit form of $f_{ij}(a, r)$ in Eq. (39). In the circular and equatorial orbit, we have

$$
v^r = 0,
$$

(B.33a)

$$
v^\theta = 0.
$$

(B.33b)

Furthermore, if p^μ, $S^{\mu\nu}$ and $J^{\alpha\beta\gamma\delta}$ take the form described in Sec. 2, we have

$$
\mathcal{Q}^{\theta\mu\nu} = 0,
$$

(B.34a)

$$
\mathcal{J}^{\alpha\mu\nu\theta} = 0.
$$

(B.34b)

Hence, operators $\mathcal{O}^{\mu\nu}$ and $\mathcal{H}^{\mu\nu}$ become

$$\mathcal{O}^{\mu\nu} = (-\omega^2 \mathcal{J}^{t\mu\nu t} + 2m\omega \mathcal{J}^{t\mu\nu\phi} - m^2 \mathcal{J}^{\phi\mu\nu\phi}$$
$$- i\omega \mathcal{Q}^{t\mu\nu} + im\mathcal{Q}^{\phi\mu\nu} + \mathcal{P}^{\mu\nu})$$
$$+ (2i\omega \mathcal{J}^{t\mu\nu r} - 2im\mathcal{J}^{r\mu\nu\phi} - \mathcal{Q}^{r\mu\nu})\partial_r$$
$$+ \mathcal{J}^{r\mu\nu r} \partial_r^2, \tag{B.35}$$

$$\mathcal{H}^{\mu\nu} = i(2\omega \mathcal{J}^{t\mu\nu r} - 2m\mathcal{J}^{r\mu\nu\phi} + i\mathcal{Q}^{r\mu\nu}) + 2\mathcal{J}^{r\mu\nu r}\partial_r. \tag{B.36}$$

We will prove that Eq. (A.20) can be rewritten as following form

$$Z_{lm\omega}^{\infty,H} = C_{lm\omega}^{\infty,H} \int dt e^{i(\omega t - m\phi)} (\sum_i \theta_i C_{ilm\omega}^{up,in}(a,r)) \tag{B.37}$$

as the first step, where $\theta_i = (m_b, S^\theta, M^{rr}, M^{r\phi}, M^{\phi\phi})$. Note that

$$S^\mu = S^\theta \delta_\theta^\mu, \tag{B.38}$$
$$M^{\mu\nu} = M^{rr}\delta_r^\mu \delta_r^\nu + M^{r\phi}(\delta_r^\mu \delta_\phi^\nu + \delta_\phi^\mu \delta_r^\nu)$$
$$+ M^{\phi\phi}\delta_\phi^\mu \delta_\phi^\nu \tag{B.39}$$

indicate $S^{\mu\nu} = S^z \hat{S}^{\mu\nu}$ and

$$J^{\alpha\beta\gamma\delta} = M^{rr}\hat{J}_3^{\alpha\beta\gamma\delta} + M^{r\phi}\hat{J}_4^{\alpha\beta\gamma\delta} + M^{\phi\phi}\hat{J}_5^{\alpha\beta\gamma\delta}, \tag{B.40}$$

where

$$\hat{S}^{\mu\nu} = \epsilon^{\mu\nu}_{\ \ \gamma r} v^\gamma,$$
$$\hat{J}_3^{\alpha\beta\gamma\delta} = -\frac{3}{m^2} p^{[\alpha}\delta_r^{\beta]}\delta_r^{[\gamma} p^{\delta]},$$
$$\hat{J}_4^{\alpha\beta\gamma\delta} = -\frac{3}{m^2}(p^{[\alpha}\delta_r^{\beta]}\delta_\phi^{[\gamma} p^{\delta]} + p^{[\alpha}\delta_\phi^{\beta]}\delta_r^{[\gamma} p^{\delta]}),$$
$$\hat{J}_5^{\alpha\beta\gamma\delta} = -\frac{3}{m^2} p^{[\alpha}\delta_\phi^{\beta]}\delta_\phi^{[\gamma} p^{\delta]}. \tag{B.41}$$

Similarly, we can get

$$\mathcal{P}^{\mu\nu} = m_b \mathcal{P}_1^{\mu\nu} + S^z \mathcal{P}_2^{\mu\nu} + M^{rr}\mathcal{P}_3^{\mu\nu}$$
$$+ M^{r\phi}\mathcal{P}_4^{\mu\nu} + M^{\phi\phi}\mathcal{P}_5^{\mu\nu}, \tag{B.42}$$
$$\mathcal{Q}^{\delta\mu\nu} = S^z \mathcal{Q}_2^{\delta\mu\nu} + M^{rr}\mathcal{Q}_3^{\delta\mu\nu} + M^{r\phi}\mathcal{Q}_4^{\delta\mu\nu}$$
$$+ M^{\phi\phi}\mathcal{Q}_5^{\delta\mu\nu}, \tag{B.43}$$
$$\mathcal{J}^{\delta\mu\nu\rho} = M^{rr}\mathcal{J}_3^{\delta\mu\nu\rho} + M^{r\phi}\mathcal{J}_4^{\delta\mu\nu\rho} + M^{\phi\phi}\mathcal{J}_5^{\delta\mu\nu\rho} \tag{B.44}$$

where

$$\mathcal{P}_1^{\mu\nu} = v^\mu v^\nu, \tag{B.45}$$
$$\mathcal{P}_2^{\mu\nu} = \Gamma^\mu_{\ \delta\rho}\hat{S}^{\nu\rho}v^\delta, \tag{B.46}$$

$$\mathcal{P}_i^{\mu\nu} = \frac{1}{3}J_i^{\mu\delta\rho\gamma} R^\nu_{\ \delta\rho\gamma} - \frac{2}{3}\Gamma^\mu_{\ \delta\rho}\Gamma^\nu_{\ \gamma\sigma}J_i^{\delta\gamma\rho\sigma}$$
$$- \frac{2}{3}(2\Gamma^{\mu\delta}_{\ \ \rho}\Gamma_{\gamma\delta\sigma}J_i^{\nu(\rho\gamma)\sigma} + J_i^\mu_{\ \delta\rho\gamma}\partial^\gamma \Gamma^{\nu\delta\rho}),$$
$$i = 3, 4, 5, \tag{B.47}$$
$$\mathcal{Q}_1^{\delta\mu\nu} = -\hat{S}^{\delta\mu}v^\nu, \tag{B.48}$$
$$\mathcal{Q}_2^{\delta\mu\nu} = -\frac{2}{3}(J_i^{\rho\mu\nu\gamma}\Gamma^\delta_{\ \rho\gamma} + 2J_i^{\rho\delta\gamma\mu}\Gamma^\nu_{\ \gamma\rho}),$$
$$i = 3, 4, 5, \tag{B.49}$$
$$\tag{B.50}$$
$$\mathcal{J}^{\delta\mu\nu\rho} = -\frac{2}{3}J_i^{\delta\mu\nu\rho}, i = 3, 4, 5. \tag{B.51}$$

From Eq. (B.35), Eq. (B.36) and Eq. (A.30), operators $\mathcal{O}^{\mu\nu}$, $\mathcal{H}^{\mu\nu}$ and $\mathcal{K}$ also have the separation form

$$\mathcal{O}^{\mu\nu} = m_b \mathcal{O}_1^{\mu\nu} + S^z \mathcal{O}_2^{\mu\nu} + M^{rr}\mathcal{O}_3^{\mu\nu}$$
$$+ M^{r\phi}\mathcal{O}_4^{\mu\nu} + M^{\phi\phi}\mathcal{O}_5^{\mu\nu}, \tag{B.52}$$
$$\mathcal{H}^{\mu\nu} = S^z \mathcal{H}_2^{\mu\nu} + M^{rr}\mathcal{H}_3^{\mu\nu} + M^{r\phi}\mathcal{H}_4^{\mu\nu}$$
$$+ M^{\phi\phi}\mathcal{H}_5^{\mu\nu}, \tag{B.53}$$
$$\mathcal{K}^{\mu\nu} = M^{rr}\mathcal{K}_3^{\mu\nu} + M^{r\phi}\mathcal{K}_4^{\mu\nu} + M^{\phi\phi}\mathcal{K}_5^{\mu\nu} \tag{B.54}$$

with

$$\mathcal{O}_1^{\mu\nu} = \mathcal{P}_1^{\mu\nu}, \tag{B.55}$$
$$\mathcal{O}_2^{\mu\nu} = -i\omega \mathcal{Q}_2^{t\mu\nu} + im\mathcal{Q}_2^{\phi\mu\nu} + \mathcal{P}_2^{\mu\nu} - \mathcal{Q}_2^{r\mu\nu}\partial_r, \tag{B.56}$$
$$\mathcal{O}_i^{\mu\nu} = (-\omega^2 \mathcal{J}_k^{t\mu\nu t} + 2m\omega \mathcal{J}_k^{t\mu\nu\phi} - m^2 \mathcal{J}_k^{\phi\mu\nu\phi}$$
$$- i\omega \mathcal{Q}_k^{t\mu\nu} + im\mathcal{Q}_k^{\phi\mu\nu} + \mathcal{P}_k^{\mu\nu})$$
$$+ (2i\omega \mathcal{J}_k^{t\mu\nu r} - 2im\mathcal{J}_k^{r\mu\nu\phi} - \mathcal{Q}_k^{r\mu\nu})\partial_r$$
$$+ \mathcal{J}_k^{r\mu\nu r}\partial_r^2, k = 3, 4, 5, \tag{B.57}$$
$$\mathcal{H}_2^{\mu\nu} = -\mathcal{Q}_2^{r\mu\nu}, \tag{B.58}$$
$$\mathcal{H}_k^{\mu\nu} = i(2\omega \mathcal{J}_k^{t\mu\nu r} - 2m\mathcal{J}_k^{r\mu\nu\phi} + i\mathcal{Q}_K^{r\mu\nu})$$
$$+ 2\mathcal{J}_k^{r\mu\nu r}\partial_r, k = 3, 4, 5, \tag{B.59}$$
$$\mathcal{K}_k^{\mu\nu} = \mathcal{J}_k^{r\mu\nu r}, k = 3, 4, 5. \tag{B.60}$$

Then we can prove Eq. (B.37), and coefficients $C_{ilm\omega}^{up,in}$ read

$$C_{1lm\omega}^{up,in} = \left(\frac{dt}{d\lambda}\right)^{-1} \left(\mathcal{O}_1^{\mu\nu}[f_{\mu\nu}^0] - \mathcal{O}_1^{\mu\nu}[f_{\mu\nu}^1]\frac{d}{dr}\right.$$
$$\left. + \mathcal{O}_1^{\mu\nu}[f_{\mu\nu}^2]\frac{d}{dr}\right) R_{lm\omega}^{up,in}, \tag{B.61}$$

$$C_{2lm\omega}^{up,in} = \left(\frac{dt}{d\lambda}\right)^{-1} \left(\mathcal{O}_2^{\mu\nu}[f_{\mu\nu}^0] + \left(-\mathcal{O}_2^{\mu\nu}[f_{\mu\nu}^1]\right.\right.$$
$$\left. + \mathcal{H}_2^{\mu\nu}[f_{\mu\nu}^0]\right)\frac{d}{dr} + \left(\mathcal{O}_2^{\mu\nu}[f_{\mu\nu}^2] - \mathcal{H}_2^{\mu\nu}\right)\frac{d}{dr}$$
$$\left. + \mathcal{H}_2^{\mu\nu}[f_{\mu\nu}^2]\frac{d}{dr}\right) R_{lm\omega}^{up,in}, \tag{B.62}$$

$$
\begin{aligned}
C^{\text{up,in}}_{klm\omega} = \left(\frac{dt}{d\lambda}\right)^{-1} \Bigg(&\mathcal{O}^{\mu\nu}_k \left[f^0_{\mu\nu}\right] \\
&+ \left(\mathcal{O}^{\mu\nu}_k \left[f^1_{\mu\nu}\right] + \mathcal{H}^{\mu\nu}_k \left[f^0_{\mu\nu}\right]\right)\frac{d}{dr} \\
&+ \left(\mathcal{O}^{\mu\nu}_k \left[f^2_{\mu\nu}\right] - \mathcal{H}^{\mu\nu}_k \left[f^1_{\mu\nu}\right] + \mathcal{K}^{\mu\nu}_k \left[f^0_{\mu\nu}\right]\right)\frac{d^2}{dr^2} \\
&+ \left(\mathcal{H}^{\mu\nu}_k \left[f^2_{\mu\nu}\right] - \mathcal{K}^{\mu\nu}_k \left[f^1_{\mu\nu}\right]\right)\frac{d^3}{dr^3} \\
&+ \left(\mathcal{K}^{\mu\nu}_k \left[f^2_{\mu\nu}\right]\right)\frac{d^4}{dr^4} \Bigg) R^{\text{up,in}}_{lm\omega}, \, k = 3, 4, 5. \quad \text{(B.63)}
\end{aligned}
$$

Then, following the Eqs. (30)–(36), the total GW energy flux reads

$$
\begin{aligned}
\mathcal{F} = &\sum_{l=2}^{\infty}\sum_{m=1}^{l}(2\pi/(m\hat{\Omega})^2) \\
&\sum_{i=1}^{5}(|\theta_i C^{\text{H}}_{lm\hat{\Omega}} C^{\text{in}}_{ilm\hat{\Omega}}|^2 + \alpha_{lm}|\theta_i C^{\infty}_{lm\hat{\Omega}} C^{\text{up}}_{ilm\hat{\Omega}}|^2) \\
= &\sum_{i=1}^{5}\sum_{j=1}^{5}\theta_i\theta_j\left(\sum_{l=2}^{\infty}\sum_{m=1}^{l}\frac{2\pi}{(m\hat{\Omega})^2}\right. \\
&\left\{\left[(C^{\text{H}}_{lm\hat{\Omega}} C^{\text{in}}_{ilm\hat{\Omega}}) \diamond (C^{\text{H}}_{lm\hat{\Omega}} C^{\text{in}}_{jlm\hat{\Omega}})\right]\right. \\
&\left.\left.+\alpha_{lm}\left[(C^{\infty}_{lm\hat{\Omega}} C^{\text{up}}_{ilm\hat{\Omega}}) \diamond (C^{\infty}_{lm\hat{\Omega}} C^{\text{up}}_{jlm\hat{\Omega}})\right]\right\}\right) \quad \text{(B.64)}
\end{aligned}
$$

where the operator $\diamond$ is defined by

$$
a \diamond b = \text{Re}(a)\text{Re}(b) + \text{Im}(a)\text{Im}(b) \quad \text{(B.65)}
$$

with Re and Im denote the real and imaginary part of a complex value, respectively. Note that use Eq.(B.37) we can also obtain a separation form for the b-EMRI waveform

$$
\begin{aligned}
h_{lm} = -\frac{2}{R}\sum_i \theta_i &\left\{\frac{2\pi}{(m\hat{\Omega})^2}C^{\text{H}}_{lm\hat{\Omega}} C^{\text{in}}_{ilm\hat{\Omega}}[a, r(t)]\right\} \\
&S^{a\hat{\Omega}}_{lm}(\Theta)e^{im[\Phi-\phi(\hat{t})]}. \quad \text{(B.66)}
\end{aligned}
$$

References

1. B.P. Abbott et al., Phys. Rev. Lett. **116**, 061102 (2016). https://doi.org/10.1103/PhysRevLett.116.061102
2. S.E. Perkins, N. Yunes, E. Berti, Phys. Rev. D **103**, 044024 (2021). https://doi.org/10.1103/PhysRevD.103.044024
3. L. Barack, A. Pound, Rep. Prog. Phys. **82**(1), 016904 (2018). https://doi.org/10.1088/1361-6633/aae552
4. P. Amaro-Seoane et al., Laser interferometer space antenna (2017). https://doi.org/10.48550/arXiv.1702.00786
5. W.R. Hu, Y.L. Wu, Natl. Sci. Rev. **4**(5), 685 (2017). https://doi.org/10.1093/nsr/nwx116
6. J.R. Gair, S. Babak, A. Sesana, P. Amaro-Seoane, E. Barausse, C.P.L. Berry, E. Berti, C. Sopuerta, J. Phys. Conf. Ser. **840**(1), 012021 (2017). https://doi.org/10.1088/1742-6596/840/1/012021
7. S. Babak, J. Gair, A. Sesana, E. Barausse, C.F. Sopuerta, C.P.L. Berry, E. Berti, P. Amaro-Seoane, A. Petiteau, A. Klein, Phys. Rev. D **95**, 103012 (2017). https://doi.org/10.1103/PhysRevD.95.103012
8. P. Amaro-Seoane et al., Living Rev. Relativ. **26**(1), 2 (2023). https://doi.org/10.1007/s41114-022-00041-y
9. P. Amaro-Seoane, J.R. Gair, M. Freitag, M.C. Miller, I. Mandel, C.J. Cutler, S. Babak, Class. Quantum Gravity **24**(17), R113 (2007). https://doi.org/10.1088/0264-9381/24/17/R01
10. J.R. Gair, C. Tang, M. Volonteri, Phys. Rev. D **81**, 104014 (2010). https://doi.org/10.1103/PhysRevD.81.104014
11. T. Hinderer, E.E. Flanagan, Phys. Rev. D **78**, 064028 (2008). https://doi.org/10.1103/PhysRevD.78.064028
12. C.F. Sopuerta, N. Yunes, Phys. Rev. D **80**, 064006 (2009). https://doi.org/10.1103/PhysRevD.80.064006
13. N. Yunes, P. Pani, V. Cardoso, Phys. Rev. D **85**, 102003 (2012). https://doi.org/10.1103/PhysRevD.85.102003
14. P. Pani, V. Cardoso, L. Gualtieri, Phys. Rev. D **83**, 104048 (2011). https://doi.org/10.1103/PhysRevD.83.104048
15. E. Barausse, N. Yunes, K. Chamberlain, Phys. Rev. Lett. **116**, 241104 (2016). https://doi.org/10.1103/PhysRevLett.116.241104
16. K. Chamberlain, N. Yunes, Phys. Rev. D **96**, 084039 (2017). https://doi.org/10.1103/PhysRevD.96.084039
17. V. Cardoso, G.M.C. Castro, A. Maselli, Phys. Rev. Lett. **121**, 251103 (2018). https://doi.org/10.1103/PhysRevLett.121.251103
18. N.A. Collins, S.A. Hughes, Phys. Rev. D **69**, 124022 (2004). https://doi.org/10.1103/PhysRevD.69.124022
19. S.J. Vigeland, S.A. Hughes, Phys. Rev. D **81**, 024030 (2010). https://doi.org/10.1103/PhysRevD.81.024030
20. C.P.L. Berry, S.A. Hughes, C.F. Sopuerta, A.J.K. Chua, A. Heffernan, K. Holley-Bockelmann, D.P. Mihaylov, M.C. Miller, A. Sesana, The unique potential of extreme mass-ratio inspirals for gravitational-wave astronomy. (2019). https://doi.org/10.48550/arXiv.1903.03686
21. E. Addison, M. Gracia-Linares, P. Laguna, S.L. Larson, Gen. Relativ. Gravit. **51**(3), 38 (2019). https://doi.org/10.1007/s10714-019-2523-4
22. X. Chen, W.B. Han, Commun. Phys. **1**(1), 53 (2018). https://doi.org/10.1038/s42005-018-0053-0
23. X. Chen, S. Li, Z. Cao, Mon. Not. Roy. Astron. Soc. Lett. **485**(1), L141 (2019). https://doi.org/10.1093/mnrasl/slz046
24. P. Amaro-Seoane, L. Santamaría, Astrophys. J. **722**(2), 1197 (2010). https://doi.org/10.1088/0004-637X/722/2/1197
25. A. Sesana, Phys. Rev. Lett. **116**, 231102 (2016). https://doi.org/10.1103/PhysRevLett.116.231102
26. W.B. Han, X. Chen, Mon. Not. Roy. Astron. Soc. Lett. **485**(1), L29 (2019). https://doi.org/10.1093/mnrasl/slz021
27. X. Zhang, X. Chen, Mon. Not. Roy. Astron. Soc. **521**(2), 2919 (2023). https://doi.org/10.1093/mnras/stad728
28. V. Cardoso, F. Duque, G. Khanna, Phys. Rev. D **103**, L081501 (2021). https://doi.org/10.1103/PhysRevD.103.L081501
29. X. Chen, Z. Zhang, Phys. Rev. D **106**, 103040 (2022). https://doi.org/10.1103/PhysRevD.106.103040
30. W. Tulczyjew, Acta Phys. Polon. **18**, 393 (1959)
31. W.G. Dixon, Nuovo Cim **34**, 317–339 (1964). https://doi.org/10.1007/BF02734579
32. W.G. Dixon, H. Bondi, Proc. Roy. Soc. Lond. A Math. Phys. Sci. **314**(1519), 499 (1970). https://doi.org/10.1098/rspa.1970.0020
33. W.G. Dixon, A. Hewish, Proc. Roy. Soc. Lond. A Math. Phys. Sci. **319**(1539), 509 (1970). https://doi.org/10.1098/rspa.1970.0191
34. H. Yu, Y. Wang, B. Seymour, Y. Chen, Phys. Rev. D **104**, 103011 (2021). https://doi.org/10.1103/PhysRevD.104.103011

35. A. Torres-Orjuela, X. Chen, P. Amaro-Seoane, Phys. Rev. D **101**, 083028 (2020). https://doi.org/10.1103/PhysRevD.101.083028
36. K.W.K. Wong, V. Baibhav, E. Berti, Mon. Not. Roy. Astron. Soc. **488**(4), 5665 (2019). https://doi.org/10.1093/mnras/stz2077
37. I. Bartos, B. Kocsis, Z. Haiman, S. Márka, Astrophys. J. **835**(2), 165 (2017). https://doi.org/10.3847/1538-4357/835/2/165
38. N.C. Stone, B.D. Metzger, Z. Haiman, Mon. Not. Roy. Astron. Soc. **464**(1), 946 (2016). https://doi.org/10.1093/mnras/stw2260
39. B. McKernan, K.E.S. Ford, J. Bellovary, N.W.C. Leigh, Z. Haiman, B. Kocsis, W. Lyra, M.M.M. Low, B. Metzger, M. O'Dowd, S. Endlich, D.J. Rosen, Astrophys. J. **866**(1), 66 (2018). https://doi.org/10.3847/1538-4357/aadae5
40. G.F. Kennedy, Y. Meiron, B. Shukirgaliyev, T. Panamarev, P. Berczik, A. Just, R. Spurzem, Mon. Not. Roy. Astron. Soc. **460**(1), 240 (2016). https://doi.org/10.1093/mnras/stw908
41. M. MacLeod, D.N.C. Lin, Astrophys. J. **889**(2), 94 (2020). https://doi.org/10.3847/1538-4357/ab64db
42. J. Steinhoff, D. Puetzfeld, Phys. Rev. D **81**, 044019 (2010). https://doi.org/10.1103/PhysRevD.81.044019
43. J. Steinhoff, D. Puetzfeld, Phys. Rev. D **86**, 044033 (2012). https://doi.org/10.1103/PhysRevD.86.044033
44. M. Rahman, A. Bhattacharyya, Phys. Rev. D **107**, 024006 (2023). https://doi.org/10.1103/PhysRevD.107.024006
45. G.A. Piovano, A. Maselli, P. Pani, Phys. Rev. D **102**, 024041 (2020). https://doi.org/10.1103/PhysRevD.102.024041
46. T. Hinderer, A. Buonanno, A.H. Mroué, D.A. Hemberger, G. Lovelace, H.P. Pfeiffer, L.E. Kidder, M.A. Scheel, B. Szilagyi, N.W. Taylor, S.A. Teukolsky, Phys. Rev. D **88**, 084005 (2013). https://doi.org/10.1103/PhysRevD.88.084005
47. J. Ehlers, E. Rudolph, Gen. Relat. Gravit. **8**, 197–217 (1977). https://doi.org/10.1007/BF00763547
48. S.A. Hughes, N. Warburton, G. Khanna, A.J.K. Chua, M.L. Katz, Phys. Rev. D **103**, 104014 (2021). https://doi.org/10.1103/PhysRevD.103.104014
49. S.A. Teukolsky, APJ **185**, 635 (1973). https://doi.org/10.1086/152444
50. I. Stakgold, M. Holst, *One-Dimensional Boundary Value Problems* (Wiley, New York, 2011), pp.185–222. https://doi.org/10.1002/9780470906538.ch3
51. Y. Mino, M. Sasaki, M. Shibata, H. Tagoshi, T. Tanaka, Prog. Theor. Phys. Suppl. **128**, 1 (1997). https://doi.org/10.1143/PTPS.128.1
52. S.A. Teukolsky, W.H. Press, APJ **193**, 443 (1974). https://doi.org/10.1086/153180
53. S.A. Hughes, Phys. Rev. D **61**, 084004 (2000). https://doi.org/10.1103/PhysRevD.61.084004
54. W.B. Han, Class. Quantum Gravity **33**(6), 065009 (2016). https://doi.org/10.1088/0264-9381/33/6/065009
55. Y. Jiang, W.B. Han, Sci. China-Phys. Mech. Astron. (2024). https://doi.org/10.1007/s11433-024-2366-5
56. S. Mano, H. Suzuki, E. Takasugi, Prog. Theor. Phys. **95**(6), 1079 (1996). https://doi.org/10.1143/PTP.95.1079
57. R. Fujita, H. Tagoshi, Prog. Theor. Phys. **112**(3), 415 (2004). https://doi.org/10.1143/PTP.112.415
58. R. Fujita, H. Tagoshi, Prog. Theor. Phys. **113**(6), 1165 (2005). https://doi.org/10.1143/PTP.113.1165
59. M. Sasaki, T. Nakamura, Prog. Theor. Phys. **67**(6), 1788 (1982). https://doi.org/10.1143/PTP.67.1788
60. B.S. Sathyaprakash, S.V. Dhurandhar, Phys. Rev. D **44**, 3819 (1991). https://doi.org/10.1103/PhysRevD.44.3819
61. T. Damour, B.R. Iyer, B.S. Sathyaprakash, Phys. Rev. D **57**, 885 (1998). https://doi.org/10.1103/PhysRevD.57.885
62. S.A. Usman, A.H. Nitz, I.W. Harry, C.M. Biwer, D.A. Brown, M. Cabero, C.D. Capano, T.D. Canton, T. Dent, S. Fairhurst, M.S. Kehl, D. Keppel, B. Krishnan, A. Lenon, A. Lundgren, A.B. Nielsen, L.P. Pekowsky, H.P. Pfeiffer, P.R. Saulson, M. West, J.L. Willis, Class. Quantum Gravity **33**(21), 215004 (2016). https://doi.org/10.1088/0264-9381/33/21/215004
63. R. Abbott et al., Phys. Rev. X **13**, 041039 (2023). https://doi.org/10.1103/PhysRevX.13.041039
64. T.L.S. Collaboration, the Virgo Collaboration, the KAGRA Collaboration, R. Abbott et al., Tests of general relativity with GWTC-3. (2021). https://doi.org/10.48550/arXiv.2112.06861
65. K. Belczynski, A. Heger, W. Gladysz, A.J. Ruiter, S.E. Woosley, G. Wiktorowicz, H.Y. Chen, T. Bulik, R. O'Shaughnesy, D.E. Holz, C.L. Fryer, E. Berti, Astron. Astrophys. **594** (2016). https://doi.org/10.1051/0004-6361/201628980
66. L. Lindblom, B.J. Owen, D.A. Brown, Phys. Rev. D **78**, 124020 (2008). https://doi.org/10.1103/PhysRevD.78.124020
67. C.J. Moore, E. Finch, R. Buscicchio, D. Gerosa, iScience **24**(6), 102577 (2021). https://doi.org/10.1016/j.isci.2021.102577